

---

# Linear-superelastic Ti-Nb nanocomposite alloys with ultralow modulus via high-throughput phase field simulation and design

Yuquan Zhu<sup>1</sup>, Tao Xu<sup>1,2\*</sup>, and Tong-Yi Zhang<sup>1\*\*</sup>

<sup>1</sup>*Materials Genome Institute, Shanghai University, Shanghai 200444, China*

<sup>2</sup>*Ningbo Institute of Materials Technology and Engineering, Chinese Academy of Sciences, Ningbo 315201, China*

## Abstract

Controlled design of the martensitic transformations (MTs) to achieve specific properties is crucial for various new applications of shape memory alloys in advanced technologies. Here, a continuum phase field model is developed to investigate a large number of Ti-Nb nanocomposites composed of Nb-rich matrix and Nb-lean nanoparticles and characterize their fundamental MTs behaviors for metallic biomaterials. Based on the high-throughput calculations, we obtain the dataset of the mechanical properties of the constructed nanocomposites and a promising candidate that exhibits a combination of unprecedented mechanical properties including ultralow modulus, linear super-elasticity and nearly free-hysteresis is designed. The exceptional mechanical properties in the nanocomposite originate from the optimized continuous martensitic transformation rather than a sharp first-order transition as that occur in typical SMAs. This work provides a new computational approach and design concept for developing novel functional materials with extraordinary properties.

---

## 1 Introduction

Titanium-based shape memory alloys (SMAs), such as Ti-Nb alloys, are an important class of smart materials that possess shape memory effect (SME) and pseudoelasticity (PE) [1], as well as high specific strength, excellent corrosion resistance, superior biocompatibility [2][3], etc. These fascinating merits are widely exploited for applications in industrial use [4] and biomedicine [5]. The SME and PE originate from the temperature- or stress-induced reversible martensitic transformations (MTs) [6]. Being a strong first-order structural transition [7], MTs usually suffer from a large stress-strain hysteresis that consists of an initial true elasticity stage with a high Young's modulus ( $> 80$  GPa) and a following stress-plateau associated with reversible structural transition. This can lead to low efficiency and poor position control of SMA actuators due to the large hysteresis and strong non-linearity [8]. Moreover, as potential metallic biomaterials, a low Young's modulus comparable with those of natural human bones ( $\sim 20$  GPa [9]) is essential for Ti-Nb alloys to avoid the "stress shielding effect" [10] and the resulting bone degradation originated from inhomogeneous stress distribution between the implant and the adjacent bone. Although several efforts have been made recently to optimize the mechanical responses of metallic alloys, e.g., modulation of the components and concentrations [11][12], cold rolling [13][14], mechanical cycling [15][16], defects engineering [17][18], introducing elastic-inelastic strain matching [19][20], and grain refinement [21][22], deliberately design and control of MTs for a combination of specific properties including low modulus, linear super-elasticity and free-hysteresis is still highly desired for various advanced biomedical and engineering applications.

From the perspective of Landau thermodynamic theory, many physical quantities of ferroic materials are associated with derivatives of free-energy with respect to certain thermodynamic variables. For

---

instance, the dielectric permittivity and piezoelectric coefficient of ferroelectrics are determined by second derivatives of the Gibbs free-energy density with respect to polarization [23][24], i.e., curvature of the thermodynamic energy profile. Based on this, ultrahigh piezoelectricity [24] and ultrahigh energy density dielectrics with minimized hysteresis [25] were designed in ferroelectrics via flattening the thermodynamic energy landscape, which were achieved by judiciously introducing nanoscale structural heterogeneity or nanodomains. Such structure manipulations can be realized by the addition of dopants or the fabrication of solid solutions, as have been demonstrated in experiments[26][27]. In analogy to dielectric properties in ferroelectrics, the mechanic properties (e.g., elastic modulus) of ferroelastic metals such as SMAs are also closely related to the second derivatives of thermodynamic energy [28][29][30]. This suggests the possibility of optimizing the overall mechanical performance of SMAs as well by nanoscale structure manipulation including rational nanocomposite design in Ti-Nb alloys.

Conventionally, time-consuming experimental searches by trial-and-error process are employed to find new materials for specific applications. Computational methods can speed up these investigations and are now playing an increasingly important role in the search for new materials or structures with tailored properties and novel functionalities. The emerging approach of high-throughput (HTP) material design has been recognized as a powerful tool in this field without experimental synthesis and characterization first [31]. There have been many inspirational HTP first-principles works, from which direct links between atomic-scale information and macroscopic functionalities are established. These approaches have shown promise in the discovery of new piezoelectric and dielectric materials [32], thermoelectric materials [33], magnetic material[34], and so on. On the other hand, the origin of material properties resides in not only chemical constituent itself but also in mesoscale morphological

---

and microstructure evolutions [35]. However, mesoscale phase field simulations in a high throughput manner that allow for the investigation of microstructure effects are rather limited [36][37]. The development of HTP mesoscale calculations is not only indispensable for the accelerated characterization of microstructure evolutions but also a boost for data- and modeling-driven discovery of new materials and structures. In this work, we develop a HTP phase-field simulation framework to optimize the mechanical response of Ti-Nb SMA nanocomposite without introducing additional elements and seek the optimal microstructure with desired properties. Based on the large-scale phase-field calculations, a nanocomposite with a perfect combination of ultralow modulus, quasi-linear elasticity and near-zero hysteresis is screened out, which has great potential for applications in biomedical materials.

## 2.1 Simulation method

Ti-Nb based alloys (TNBAs) undergo diffusionless and reversible martensite transformation (MT) between cubic  $\beta$ -austenite (point group  $m\bar{3}m$ ) and orthorhombic  $\alpha'$ -martensite (point group  $mmm$ ) phases [38] during the thermomechanical loading, as shown in Fig. 1 (a). This cubic to orthorhombic MT is associated with six variants [39][40]. For simplicity, we construct 2D nanocomposite phase field model within the plane stress condition, and there are 4 variants (V1 – V4) corresponding to 4 different stress-free transformation strain (SFTS) tensors after dropping the out-of-plane strain. All the SFTSs are shown in Supporting Information. In the phase field model, a continuous structure order parameter  $\eta_i$  ( $i = 1 - 4$ ) is employed to characterize the MT phase transition, with  $\eta_i = 0$  and  $\eta_i = \pm 1$  representing austenite and  $i$ -th martensite variant, respectively [40]. The total free energy of the system  $F$  consists of the Landau free energy  $f_{ch}$ , the gradient energy  $f_{gr}$ , and the elastic energy  $f_{el}$

[41]:

$$F = \int (f_{ch} + f_{gr} + f_{el}) dV \quad (3).$$

The microstructure evolution of the MT phase transition is governed by the time-dependent Ginzburg-Landau (TDGL) equation [42]:

$$\frac{\partial \eta_i(\mathbf{r}, t)}{\partial t} = -L \frac{\delta F}{\delta \eta_i(\mathbf{r}, t)} + \zeta_i(\mathbf{r}, t), i = 1 \sim 4 \quad (2),$$

where  $L$  is the kinetic parameter and  $\zeta_i(\mathbf{r}, t)$  is the Stochastic-Langevin noise terms accounting for the effect of thermal fluctuations [43]. Full details of the simulation methods and the expressions for different energies are provided in the Supporting Information.

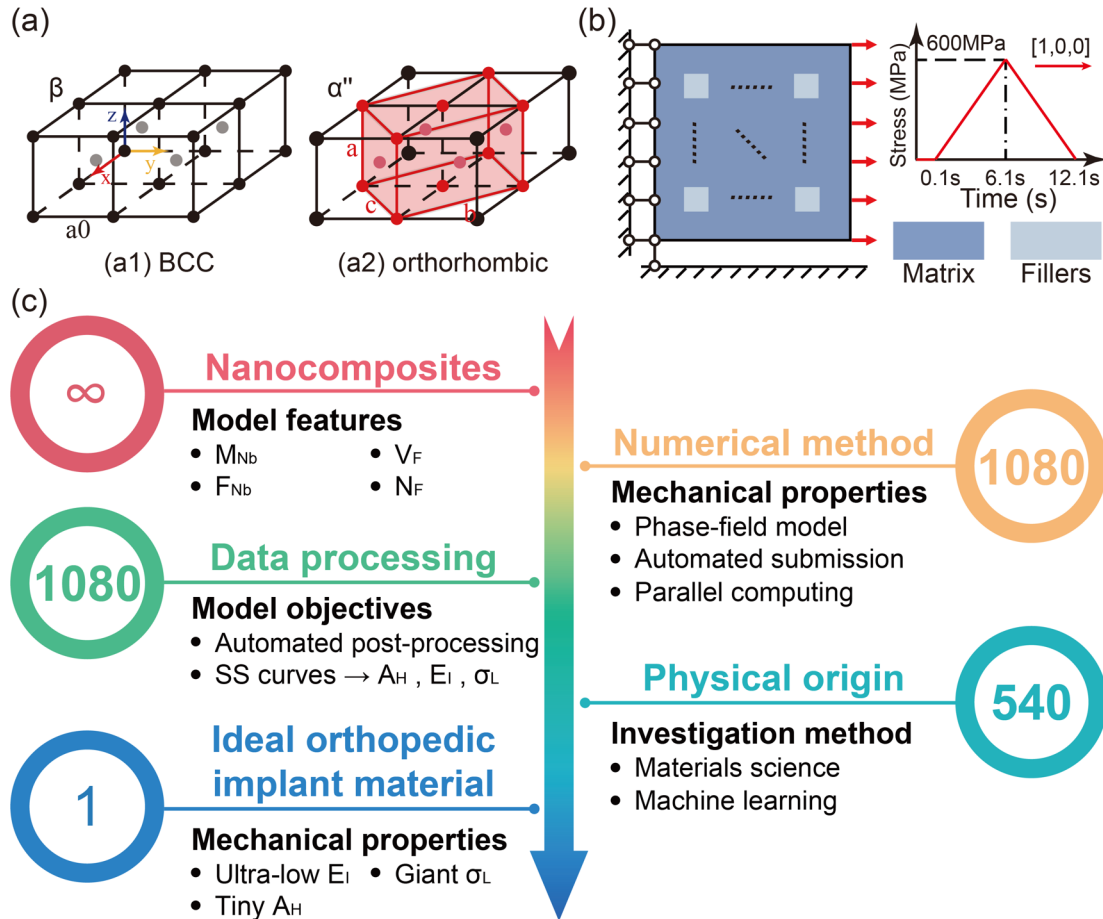


Fig. 1 (a) Crystal structure of parent (BCC) and martensitic (orthorhombic) phase (b) Distribution of Nb-lean nanoparticles in the square-array Ti-Nb nanocomposite and loading-unloading process. (c) HTP phase-field simulation framework for the Ti-Nb nanocomposite.

---

## 2.2 Model and procedure

We design a series of Ti-Nb square-array nanocomposite structures consisting of different Nb-lean nanoparticles uniformly and coherently embedded in a Nb-rich Ti-Nb alloy matrix as shown in Fig. 1 (b). The motivation for the choice of such a nanostructure is the advancements in fabrication techniques of composites and the various new phenomenon associated with them [44]. We take the Nb concentration ( $C_{\text{Nb}}$ ) of matrix ( $M_{\text{Nb}}$ ) and fillers ( $F_{\text{Nb}}$ ), volume fraction of fillers ( $V_F$ ) and number of fillers ( $N_F$ ) as four feature variables in the Ti-Nb nanocomposite. The concentration ranges of  $M_{\text{Nb}}$  and  $F_{\text{Nb}}$  are from 15% – 20% and 5% – 10%, respectively, with a 1% interval. For modeling purposes, we chose 6 groups of  $V_F$  varying from 1.56% - 56.25%, which corresponds to the total area of fillers are  $8^2\text{nm}^2$ ,  $16^2\text{nm}^2$ ,  $24^2\text{nm}^2$ ,  $32^2\text{nm}^2$ ,  $40^2\text{nm}^2$  and  $48^2\text{nm}^2$ . Correspondingly, there are 5 groups of  $N_F$  : 1, 4, 16, 36 and 64. The computational framework for the design of Ti-Nb composite is represented schematically in Fig. 1 (c). We start by specifying the above four feature variables ( $M_{\text{Nb}}$ ,  $F_{\text{Nb}}$ ,  $V_F$  and  $N_F$ ) with automatic nanocomposite modeling, which yields 1080 candidates from a combinatorial point of view. Although the nanofillers can be distributed in the matrix randomly, we restrict the fillers to a square nanocomposite structure [45], a typical archimedean lattice structures, to reduce computational complexity. Then we carry out high efficiency phase-field simulations for the established nanocomposite models and compute their microstructure evolutions as well as stress-strain (SS) curves under mechanical stress along the [100] direction. The quantitative analyses of the SS curves are subsequently conducted, and the main mechanical parameters are extracted, including the apparent incipient Young's modulus ( $E_I$ ), the elastic stress limit ( $\sigma_L$ ), and the hysteresis area ( $A_H$ ). The results are stored for further analyses and the desired configuration could be obtained based on certain screening criteria with specific application.

---

### 3.1 Overview of high-throughput phase-field results

Based on the HTP phase-field simulations, we select the range of  $N_F$  and  $V_F$  (as shown in Supporting Information) that effectively modulate the mechanical properties (a total of 540 configurations) and plot four feature variables dependence of these mechanical properties in Fig. 2, in which  $V_F$  increases from 1.56% to 39.06% on each row and  $N_F$  decrease from 64 to 4 on each column. As the map shown in Fig. 2 (a), there is a rough trend that nanocomposites with larger  $V_F$  have lower ( $E_I$ ), although the Nb-lean nanoparticle is assumed to have the same elastic constants as that of the matrix. This indicates the coupling between the components with different  $C_{Nb}$  gives rise to Young's modulus superior to their inherent ones. It is also interesting that  $F_{Nb}$  can dramatically reduce  $E_I$  when the  $F_{Nb}$  is lower ( $F_{Nb} < 8\%$ ) (see panel a3-a5, a8-a10 and a13-a15) and the  $V_F$  is higher ( $V_F > 14.06\%$ ), while  $M_{Nb}$  and  $N_F$  has negligible on  $E_I$  on the whole range of  $V_F$ . On the other hand,  $\sigma_L$  is also closely connected with these four variables. As displayed in Fig. 2 (b),  $\sigma_L$  decreases with the increasing of  $V_F$  while increase with the increasing of  $M_{Nb}$ . The opposite variation tendencies of  $E_I$  and  $\sigma_L$  with respect to the  $C_{Nb}$  of different components indicates that different components play different roles in regulating the mechanical properties of nanocomposites. Moreover, the calculated hysteresis area  $A_H$  of the nanocomposites spans a large range from 0 MJ/m<sup>3</sup> to 3 MJ/m<sup>3</sup> for different features (see Fig. 2 (c)), indicating that the embedding of filler greatly reduces the energy loss during the loading-unloading cycle. All these results indicate that the mechanical properties of nanocomposites are nonlinearly affected by all four features.

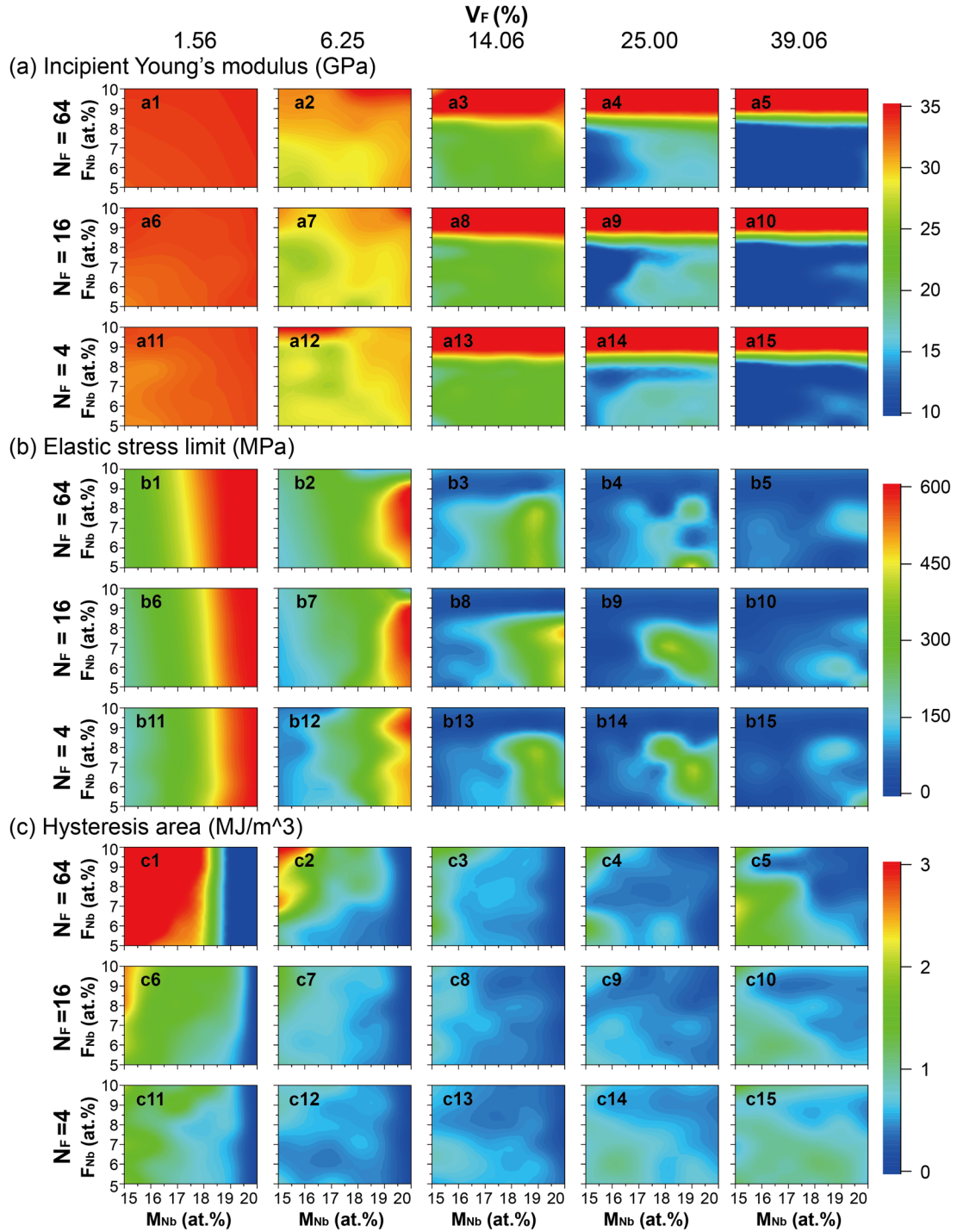


Fig. 2 Mapping results of HTP phase-field simulations of (a) the apparent incipient Young's modulus (b) the elastic stress limit and (c) the hysteresis area.

### 3.2 The effect of single nanocomposite

To further understand the physical origin of modulating the mechanical properties by altering the nanocomposite features, Fig. 3 show the SS curves obtained by the variation of one feature after



controlling three features, respectively. It can be readily seen that most of the SS curves indicate that the material exhibits a nearly zero hysteresis, and the size of the hysteresis can also be seen intuitively through the SS curves. Thus, only the  $\sigma_L$  and the  $E_I$  are highlighted in this section.

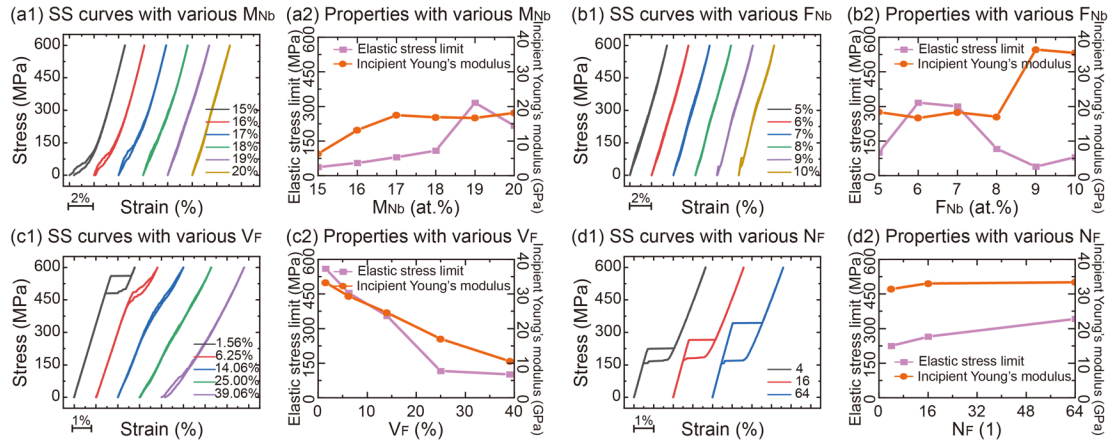


Fig. 3 Calculated SS curves and mechanical properties of nanocomposites that have (a) various  $M_{Nb}$  with  $F_{Nb} = 6\%$ ,  $V_F = 25.00\%$ ,  $N_F = 16$ ; (b) different  $F_{Nb}$  with  $M_{Nb} = 19\%$ ,  $V_F = 25.00\%$ ,  $N_F = 16$ ; (c) different  $V_F$  with  $M_{Nb} = 19\%$ ,  $F_{Nb} = 8\%$ ,  $N_F = 16$  and (d) different  $N_F$  with  $M_{Nb} = 16\%$ ,  $F_{Nb} = 8\%$ ,  $V_F = 1.56\%$ .

Fig.3 (a1) shows that the shape of the SS curves gradually converts from concave to convex with the increase of the  $M_{Nb}$ , and the mechanical properties of nanocomposites change accordingly. Therefore, as shown in Fig.3 (a2), with the increase of the  $M_{Nb}$ , the  $\sigma_L$  will first rise and then decrease with the evolution of the SS curves, and the maximum of  $\sigma_L$  is shown when the SS behavior is close to linear as  $M_{Nb} = 19\%$ . This trend of the  $\sigma_L$  reflects its nonlinearity caused by  $M_{Nb}$ . In addition, it can be seen that the  $E_I$  will increase slightly as the  $M_{Nb}$  increases. Since the decrease in  $E_I$  is caused by the continuous MT, the change in  $E_I$  indicates that the increase of  $M_{Nb}$  can restrain the spread of MT.

Fig.3 (b1) shows the SS curves alter different  $F_{Nb}$  from 5% to 10%. The samples with high-level  $F_{Nb}$  ( $> 9\%$ ) exhibit narrow hysteresis but a shorter stress plateau, which reflects the occurrence of MT is neither drastic nor continuous, and the other samples completely disappeared the hysteresis and

---

reduced the stress plateau. As shown in Fig.3 (b2), the  $E_I$  increase dramatically up to 35GPa, and the  $\sigma_L$  drops sharply below 100MPa, which reflects that there is an obvious critical stress of MT and the  $E_I$  shows the modulus (35GPa) of the austenite when  $F_{Nb} > 9\%$ . On the contrary, for the samples with lower  $F_{Nb}$  ( $<9\%$ ), since the martensite has been generated during the relaxation, external stress will promote the growth of the martensite but generally nonlinear or discontinuous growth, so the SS curve does not maintain a strict linear shape, and the  $\sigma_L$  appears a strong nonlinearity for  $F_{Nb}$ .

As shown in Fig.3 (c1), the variation of  $V_F$  lead to drastically different SS curves. For systems with less fillers embedded ( $V_F = 1.56\%$ ) shows a large stress hysteresis, austenitic modulus, and an obvious stress plateau, which are conventional characteristics of MT. However, with the increase of the  $V_F$ , the SS curves change gradually to slim ones with narrow hysteresis and obviously changes from convex curves to concave curves. Due to the  $F_{Nb} < 9\%$ , according to the previous conclusions, martensite will spontaneously generate during relaxation and will grow up with the increase of external stress. For the stress-induced MT during the loading process, the larger  $V_F$  means the stronger driving force for MT and the martensite is easier to grow. Therefore, the fast-growing martensite caused by a lager  $V_F$  effectively reduces the  $E_I$  but reduces the  $\sigma_L$  simultaneously as shown in Fig.3 (c2). It should be noted that there must be a strong linear curve ( $V_F = 25\%$ ) during the change of  $V_F$ , which has a higher  $\sigma_L$  compared to the surrounding parameters.

To investigate the  $N_F$  effect in nanocomposites, three different number of fillers are introduced as shown in Fig.3 (d1). As the  $N_F$  decrease, the obvious stress plateau gradually becomes inclined, and the hysteresis area decreases accordingly. In the previous section, it was pointed out that a decrease in the  $N_F$  would increase the local stress under the same  $V_F$  and promote the spread of the stress-induced MT. Therefore, both  $\sigma_L$  and  $E_I$  will increase slightly with the increase of  $N_F$  as shown in Fig.3 (d2), but

---

it can be seen that the modulation effect of  $N_F$  is weaker than other features.

### 3.3 The effect of coherent nanocomposite

The widely tunable and variable mechanical response of the nanocomposite are attributed to the local stress fields [46] and their distribution associated with the inserted nanoparticles. Fig. 4 (a1) plots the curves of free energy densities as a function of order parameter for Ti-Nb alloys with different Nb concentration at 300 K, in which the martensite changes gradually from a stable state to an unstable state with the increasing  $C_{Nb}$ . The  $C_{Nb}$  dependence of the SFTSs' components also indicates that the SFTS and the elastic energy density caused by MT are inversely proportional to the  $C_{Nb}$  (Fig.4 (a2)). As a result, austenite is unstable and martensite evolves spontaneously in the Nb-lean fillers ( $C_{Nb} < 8\%$ ) when the nanocomposite is quenched to room temperature, while the matrix ( $C_{Nb} \geq 8\%$ ) could not activate MT without the aid of external loads to reach the critical stress, as shown in Fig.4 (a2). Hence, the transformed filler will generate internal stress at the austenite-martensite (AM) interfaces due to the lattice mismatch (i.e.  $C_{Nb}$  dependent SFTS) between them. Assuming that the martensite phase of fillers has been nucleated and the matrix is still austenite, the internal stress at the AM interfaces generated the driving forces to promote the movement of martensite. The difference in configuration of  $M_{Nb}$  and  $F_{Nb}$  at the AM interfaces determine whether the martensite spread into matrix or be inhibited in the filler. As displayed in Fig.4 (a3), the map of driving force is divided by black line ( $M_{Nb} \approx 18\%$ ) into easy and hard to spread, which are highlighted in blue and red, respectively, and the Nb-rich matrix can obviously inhibit the spread of MT. Therefore, the  $C_{Nb}$  of fillers and matrix could influence the nucleation and spread of MT process in nanocomposites by mediating the Landau free energy densities and SFTS. On the other hand, the geometric features (i.e. number and volume fraction)

---

of the nano-fillers further mediate the strength and distribution of the generated stress field. This is verified by performing simplified simulations on nanocomposite with pre-strained fillers without considering the martensitic transition. The pre-straining is set to be the value of SFTS of the martensite. The stress field in the matrix caused by the fillers with pre-straining for various configurations are shown in Fig.4 (b) Fig.4 (c) show the distribution of local stress in the matrix generated by different number and volume fraction of fillers. We take V3 with  $F_{Nb} = 7\%$  as the example to investigate the effect of strain mismatch on the local stress field caused by the embedding of martensite fillers as show in Fig.4 (b). It can be seen from Fig.4 (c), with the increase of  $V_F$ , the local stress distribution range gradually expands correspondingly, and when the  $V_F$  is greater than 25.00%, the stress distribution forms a second peak around 400MPa. And the increase of  $V_F$  not only increases the maximum value of the local stress field (represented by the red dashed line), but also significantly increases the probability of  $\sigma \geq 600\text{MPa}$  (the assumed critical stress for martensite spread in the matrix, indicated by the blue dashed line). Moreover,  $N_F$  also regulates the distribution and probability density of local stress field. Contrary to  $V_F$ , a smaller  $N_F$  can increases the maximum value of the local stress field and the probability of  $\sigma \geq 600\text{MPa}$ . Hence, both the  $V_F$  and the  $N_F$  significantly affect the magnitude and extent of the local stress field, which consequently mediate the formation and growth of MT due to the existence of critical stress of MT.

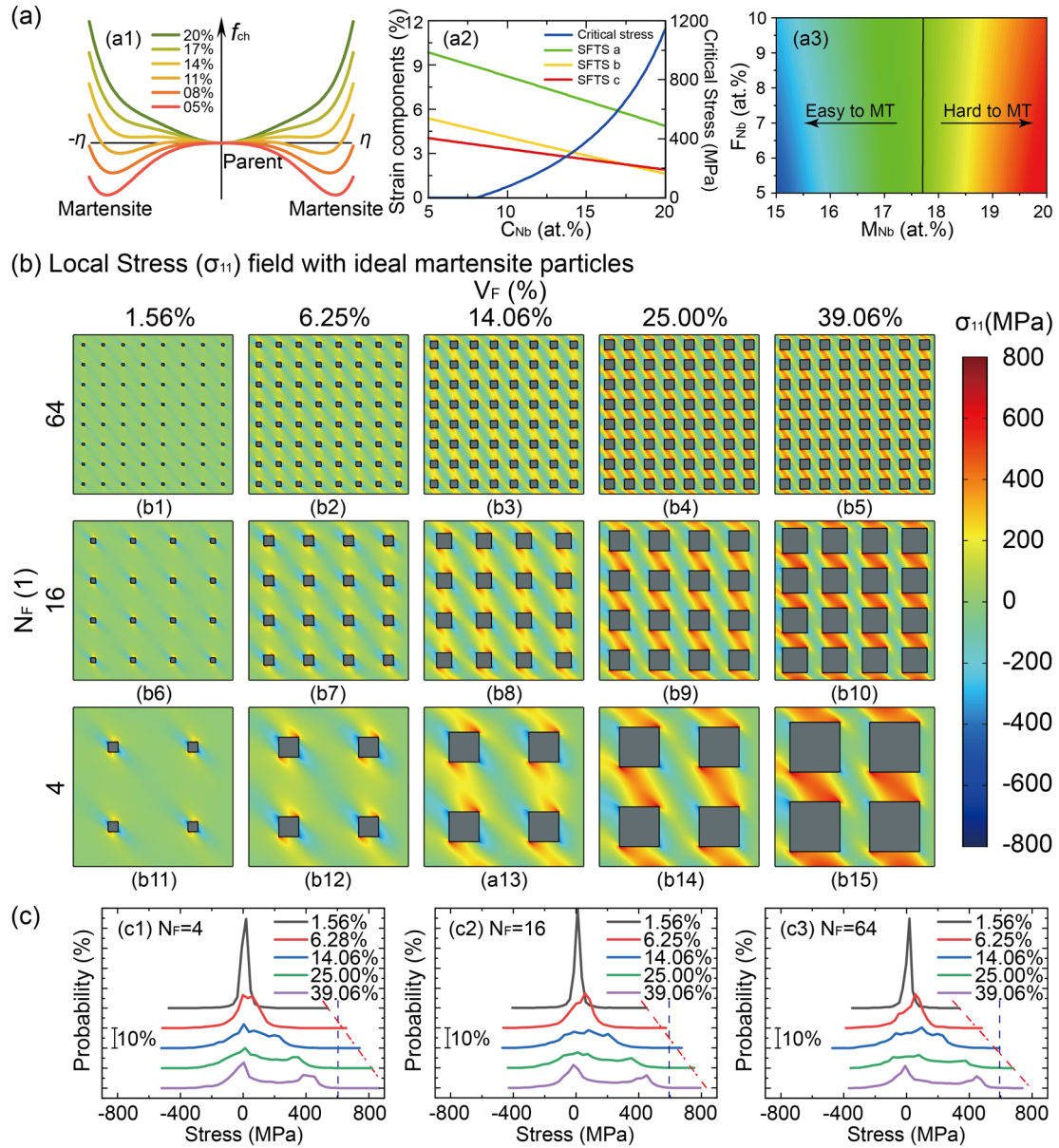


Fig. 4 Schematic diagrams for understanding the physical origin of fillers to achieve the specified properties. (a1) Landau free energy curve per unit volume, (a2) SFTS tensors component and MT critical stress under different  $C_{Nb}$  and (a3) local stress field on the [100] direction of Ti-Nb nanocomposites of different  $V_F$  and different  $N_F$  of fillers and (c) local stress field probability distribution with  $V_F = 1.56\%$ ,  $6.28\%$ ,  $14.06\%$ ,  $25.00\%$  and  $39.06\%$  for different  $N_F$ .

As previously analyzed, all 4 features are associated with mechanical properties. To have a quantitative understanding of the effect of each feature on the mechanical properties, we combine the HTP phase-field simulations with machine learning (ML) to investigate the role of nanocomposite features. A ML algorithm, Random Forest (RF) [50], was conducted on the dataset obtained previously, and the

---

performances of RF was evaluated by Leave-One-Out Cross-Validation (LOOCV). The predictive performance of RF on the testing data was measured by the correlation coefficient ( $R$ ) which are defined by

$$R = \frac{|\sum(y_i - \bar{y})(\hat{y}_i - \bar{\hat{y}})|}{\sqrt{\sum(y_i - \bar{y})^2 \sum(\hat{y}_i - \bar{\hat{y}})^2}}$$

Where  $y$ ,  $\bar{y}$  and  $\hat{y}$  represent the actual value, the average value and the predicted value. The value of  $R$  is between 0 and 1, and  $R = 1$  indicates that the predicted value is exactly the same as the actual value. Fig.5 (a1-c1) shows the predictive performance of three mechanical properties obtained by RF algorithm. As we can see, the RF has a great predictive performance for  $E_I$  ( $R = 0.9881$ ),  $\sigma_L$  ( $R = 0.9537$ ), and  $A_H$  ( $R = 0.9668$ ). Therefore, in order to further identify the importance of features, we obtained the importance of each feature in the random forest. The features importance of each mechanical properties is shown in Fig. 5 (a2-c2). The importance values of the features computed by RF indicate that the  $V_F$  plays the strongest role in achieving specific  $E_I$  and  $\sigma_L$ , and also has a strong influence on the  $A_H$ . And the  $C_{Nb}$ , including  $M_{Nb}$  and  $F_{Nb}$ , has a major effect on three mechanical properties. Since feature importance is a normalized value, although the role of  $N_F$  is very important and has been discussed, its importance is weaker than other features. This implies that when the features are coupled, the  $V_F$  plays a major role in modulating the mechanical properties of nanocomposites, and the  $C_{Nb}$ , including  $M_{Nb}$  and  $F_{Nb}$ , play a secondary role. Although the  $N_F$  can effectively adjust the distribution and probability density of local stress field to affect MT, its effect on adjusting mechanical properties is not obvious compared to other three features.

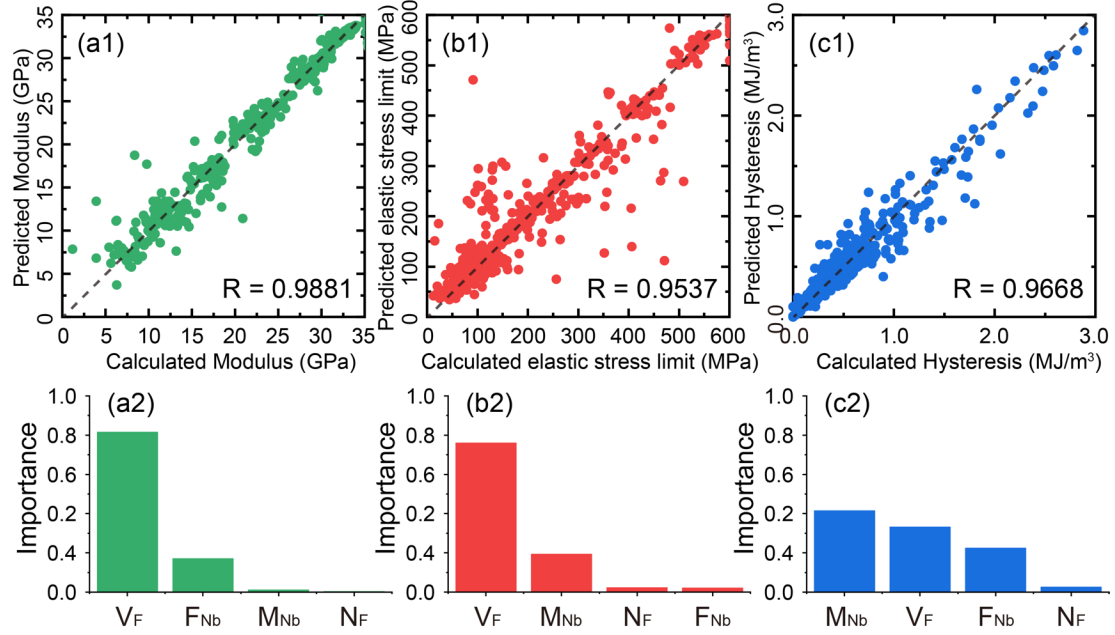


Fig. 5 The HTP phase field simulation datasets processed by ML of (a1) - (c1) predictive performance and (a2) - (c2) the ranking of feature importance of nanocomposites.

### 3.5 Ideal bone implant design strategy

The datasets of the Young's modulus and elastic stress limit of the constructed nanocomposites obtained from the high throughput simulation, together with those of Ti2448 (Ti-24Nb-4Zr-8Sn in wt.%) (denoted with a red circle), are given in Fig.6 (a). The difference of  $C_{Nb}$  between matrix and fillers in the system plays an important role in controlling MT process and regulating the corresponding mechanical properties. The  $E_I$  and elastic strain limit of the nanocomposites are widely distributed within 10GPa ~ 35GPa and 0% ~ 3%, respectively. This tunable and variable modulus indicates engineering the chemical composition and geometry of nanocomposite offers great flexibility to turn the mechanical performance of the materials. Surprisingly, a large number of nanocomposite configurations are shown to possess a lower incipient Young's modulus and a higher elastic stress limit than those of Ti2448 [51]. Based on the comprehensive HTP simulation results, we could now locate the configuration with the best compromise of lower  $E_I$  and larger  $\sigma_L$ . We then take the configuration denoted with the purple star as an example of the candidate nanocomposite for ideal bone implant

---

(IBI), to investigate the mechanical properties of the nanocomposites in detail. This designed IBI model is composed of Nb-rich TiNb matrix ( $C_{Nb} = 18\%$ ) and 25% volume fraction of Nb-lean TiNb square fillers ( $F_{Nb} = 7\%$ ), as shown in Fig.6 (b). The SS curve of IBI during loading-unloading cycle together with that of uniform bulk Ti2448 are shown in Fig.6 (c) with the red curve and gray curve, respectively. The SS curve of Ti2448 features a typical characteristic of a large stress hysteresis with an obvious stress plateau, which is consistent with experimental observations. By contrast, the stress plateau disappears completely in the SS curve of IBI and the designed nanocomposite exhibits a quasi-linear elasticity and almost hysteresis-free mechanical behavior. Moreover, as compared to Ti2448, a dramatically reduced  $E_I$  of 15.3GPa is achieved without sacrificing  $\sigma_L$  (i.e. 419MPa) in IBI. This ultralow value is even lower than the  $E_I$  of nature bones ( $\sim 20$  GPa [9]). Compared with other common bulk materials, the modulus and elastic strain limit predicted in the current study have a wide distribution, which can be applied to various applications that are difficult for conventional metals, such as bone implants to promote bone recovery. It is striking that the designed IBI exhibits a linear-superelastic with ultralow modulus, which could be the embedded filler transforms the sharp first-order MT process of TNBAs into a continuous second-order MT process.



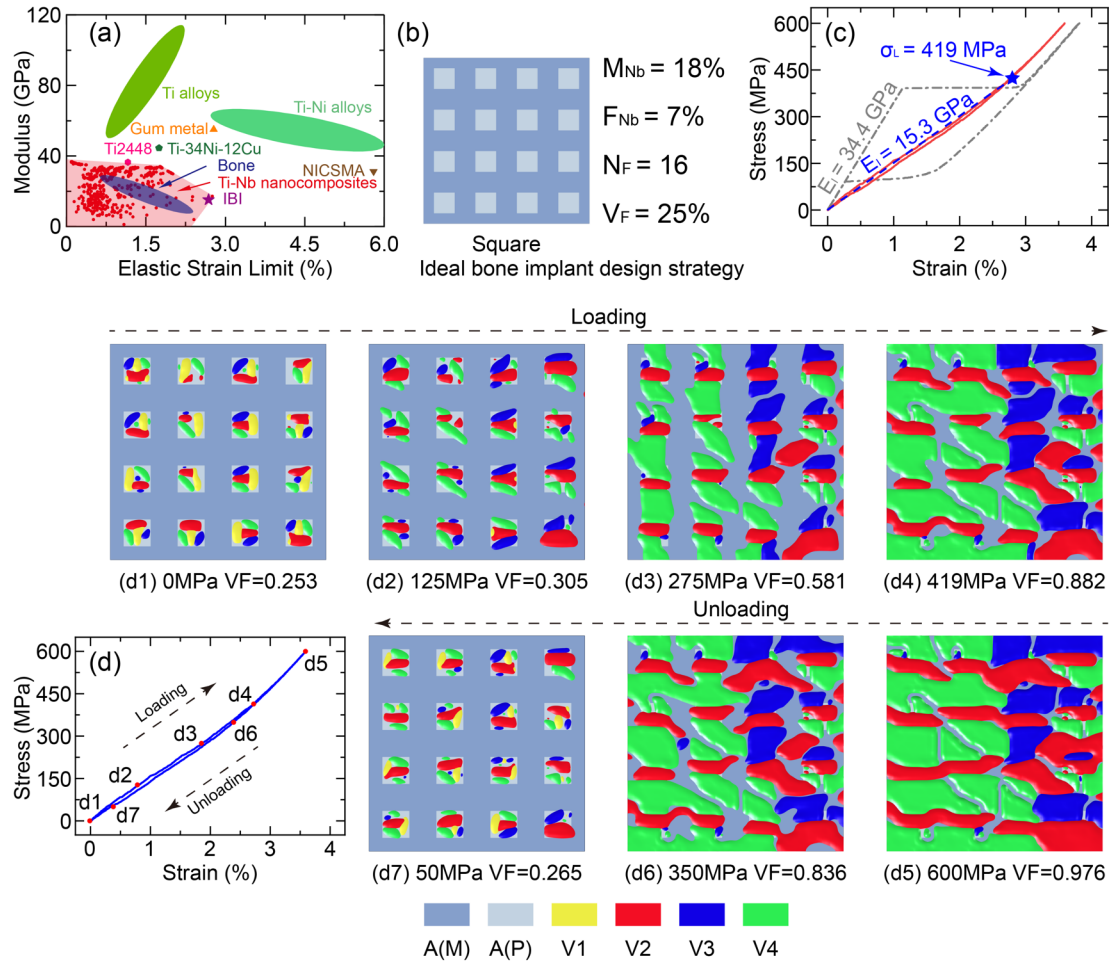


Fig. 6 (a) Comparison of the modulus and elastic strain limit between prediction from this study with those reported in the literature. (b) The microstructure of the IBI obtained from HTP phase-field simulations (c) (d) Microstructure evolution during MT in IBI during loading ((d2) ~ (d4), and unloading ((d5) ~ (d7)) process.

To gain a thorough understanding of the exceptional mechanical properties, the microstructure evolutions corresponding to the marked points of the loading-unloading SS curve are analyzed and the results are displayed in Fig.6 (d). As shown Fig.6 (d1), abundant martensitic particles exist in the nano-fillers while the matrix remains austenite phase when the nanocomposite is quenched to 300K in a stress-free configuration. This is because the critical temperature of Nb-lean fillers for martensitic transition  $M_s = 382\text{K}$  is higher than the simulation temperature. The emerged temperature-induced martensitic particles are composed of multi-variants in self-accommodating domain patterns. These martensitic particles behave as seeding beds of martensite, eliminating the nucleation barriers for MT.

---

Upon loading, the stress-induced martensite re-orientation takes place and the favored variants (variant 1 (V1), variant 2 (V2) and V3) dominate and gradually fill the fillers. These martensitic variants grow gradually and continuously into the matrix, which is significantly different from the common avalanche-like discontinuous martensitic phase transition. With increasing stress (Fig. 6 (d3) and (d4)), the existing martensitic variants continue to expand in the matrix, accompanied by the formation and merging of new martensitic configurations in the matrix as well. At the end of the loading (600 MPa), the martensitic domains spread almost over the entire area of the nanocomposite with a volume fraction of 97.6%, as illustrated in Fig.6 (d5). The remained parent phase mainly originates from martensitic variants interfaces. In the process of unloading, these remained parent phases initiate the inverse martensite to austenite transition in the matrix and the austenite spreads gradually from the matrix towards the interfaces of the nanocomposite (Fig.6 (d6)). The martensite disappears completely in the matrix when the applied stress reduces to 50 MPa (Fig. 6 (d7)) and the Nb-lean fillers also transform back to the initial self-accommodating multi-variants martensite configurations after unloading, which contributes to the zero-residual strain in a loading-unloading cycle. Therefore, the nanocomposite experiences macroscopically continuous MT throughout the loading and unloading procedure rather than a sharp first-order transition as that occur in typical SMAs, which thus exhibits linear super-elasticity and ultralow apparent Young's modulus in Fig.6 (d). The continuous characteristics of the forward and backward martensitic transitions are derived from the non-uniform distribution of stress as discussed above.

To examine the functional stability of the designed nanocomposite, the second loading-unloading cycle is performed for the IBI. The obtained SS curve and the corresponding evolution of microstructures are illustrated in Supporting Information, which coincide with those in the first one, indicating the

---

mechanical stability of the IBI. In addition, we investigate the influence of the distribution of the nanofillers on the mechanical behavior by performing calculations of triangular and honeycomb-array nanocomposites with the same constituent phases as that of IBI. As the SS curves and the corresponding microstructures and their evolutions shown in Supporting Information, the mechanical behavior of the nanocomposite is insensitive to the nanofiller distribution.

#### **4. Conclusions**

In conclusion, we have developed a phase field model to accelerate the design of optimal microstructure with desired mechanical properties. Based on our HTP phase field calculations, a Ti-Nb alloy composite with ultralow modulus, linear super-elasticity and nearly free-hysteresis has been achieved by nanocomposite structure engineering, which is promising for biomaterial applications. These superior mechanical properties attribute to the non-uniform stress confinement that facilitates continuous martensitic transitions. The proposed strategy by nano-structure engineering to improve the mechanical properties is not limited to improve the mechanical properties of ferroelastics, but is also applicable to optimize other functional properties in ferroelectric and ferromagnetic transformations for their strong similarity.

#### **ACKNOWLEDGMENTS**

The authors acknowledge financial support for Tao Xu from the National Natural Science Foundation of China (Grant No. 11802169).

\* E-mail: xutao6313@shu.edu.cn

\*\* E-mail: zhangty@shu.edu.cn

---

## Reference

- [1] Lexcelent, C. Shape-memory Alloys Handbook, John Wiley & Sons, Inc, Hoboken, NJ, USA, (2013)
- [2] Huang, W. M., Ding, Z., Wang, C. C., Wei, J., Zhao, H, Purnawali, H. Shape memory materials. *Mater. Today.*, **13(7-8)**, 54-61 (2010)
- [3] Jaronie, M. J., Martin, L., Aleksandar, S., Mark, A. G. A review of shape memory alloy research, applications and opportunities. *Mater. & Design.*, **56**, 1078-1113 (2014)
- [4] Lagoudas, D. C. Shape Memory Alloys: Modeling and Engineering Applications (2008)
- [5] Shape memory alloys for biomedical applications. *Mater. Today.*, **11(12)**, 70 (2008)
- [6] Kim, H. Y., Ikehara, Y., Kim, J. I., Hosoda, H., Miyazaki, S. Martensitic transformation, shape memory effect and superelasticity of Ti-Nb binary alloys. *Acta. Mater.*, **54(9)**, 2419-2429 (2006)
- [7] Christian, J. W. The Theory of Transformations in Metals and Alloys, Elsevier, Oxford, UK, (2002)
- [8] Villoslada, A., Flores, A., Copaci, D., Blanco, D., Moreno, L. High-displacement flexible Shape Memory Alloy actuator for soft wearable robots. *Robot. Auton. Syst.*, **73**, 91-101 (2015)
- [9] Turner, C. H., Rho, J., Takano, Y., Tsui, T. Y., Pharr, G. M. The elastic properties of trabecular and cortical bone tissues are similar: results from two microscopic measurement techniques. *J. Biomech.*, **32**, 437-441 (1999)
- [10]Kennady, M. C., Tucker, M. R., Lester, G. E., Buckley, M. J. Stress shielding effect of rigid internal fixation plates on mandibular bone grafts. a photon absorption densitometry and quantitative computerized tomographic evaluation. *Int. J. Oral. Max. Surg.*, **18(5)**, 307-310 (1989)
- [11]Wang, Q. Z., Lin, Y. G., Zhou, F., Kong, J. Z. The influence of Ni concentration on the structure, mechanical and tribological properties of Ni–CrSiN coatings in seawater. *J. Alloy. Compd.*, **819**, 152998 (2020)
- [12]Besse, M., Castany, P., Gloriant, T. Mechanisms of deformation in gum metal TNTZ-O and TNTZ titanium alloys: A comparative study on the oxygen influence. *Acta. Mater.*, **59(15)**, 5982-5988 (2011)
- [13]Ahadi, A., Matsushita, Y., Sawaguchi, T., Sun, Q. P., Tsuchiya, K. Origin of zero and negative thermal expansion in severely-formed superelastic NiTi alloy. *Acta. Mater.*, **124**, 79-92 (2017)
- [14]Tsuchiya, K., Inuzuka, M., Tomus, D., Hosokawa, A., Nakayama, H., Morii, K., Todaka, Y., Umemoto, M. Martensitic transformation in nanostructured TiNi shape memory alloy formed via severe plastic deformation. *Mat. Sci. Eng. A-Struct.*, **438**, 643-647 (2006)
- [15]Miyazaki, S., Imai, T., Igo, Y., Ostuka, K. Effect of cyclic deformation on the pseudoelasticity characteristics of Ti-Ni alloys. *Metall. Trans.*, **17A(1)**, 115-120 (1986)
- [16]Nemat-Nasser, S., Guo, W. G. Superelastic and cyclic response of NiTi SMA at various strain rates and temperatures. *Mech. Mater.*, **38(5)**, 463-474 (2006)
- [17]Rajasekaran, G., Narayanan, P., Parashar, A., Effect of Point and Line Defects on Mechanical and Thermal Properties of Graphene: A Review. *Crit. Rev. Solid. State.*, **41(1)**, 47-71 (2016)
- [18]Wang, D., Wang, Y. Z., Zhang, Z., Ren, X. B. Modeling Abnormal Strain States in Ferroelastic Systems: The Role of Point Defects. *Phys. Rev. Lett.*, **105**, 205702 (2010)
- [19]Hao, S. J., Cui, L. S., Jiang, D. Q., Han, X. D., Ren, Y., et al. A Transforming Metal Nanocomposite with Large Elastic Strain, Low Modulus, and High Strength. *Science.*, **339**, 1191 (2013)
- [20]Hamilton, R. F., Sehitoglu, H., Efstathiou, C., Maier, H. J. Mechanical response of NiFeGa alloys containing second-phase particles. *Scripta. Mater.*, **57(6)**, 497-499 (2007)
- [21]Nasiri, Z., Ghaemifar, S., Naghizadeh, M., Mirzadeh, H., Thermal mechanisms of grain refinement

- 
- in steels: a review. *Met. Mater. Int.*, 1-17 (2020)
- [22]Murty, B. S., Kori, S. A., Chakraborty, M., Grain refinement of aluminium and its alloys by heterogeneous nucleation and alloying. *Int. Mater. Rev.*, **47(1)**, 3-29 (2002)
- [23]Fu, H. X., Cohen, R. E. Polarization rotation mechanism for ultrahigh electromechanical response in single-crystal piezoelectrics. *Nature.*, **403**, 281-283 (2000)
- [24]Li, F., Lin, D. B., Chen, Z. B., Cheng, Z. X., Wang, J. L., Li. C. C., Xu, Z., et al. Ultrahigh piezoelectricity in ferroelectric ceramics by design. *Nat. Mater.*, **17(4)**, 349-354 (2018)
- [25]Park, S. E., Shrout, T. R. Ultrahigh strain and piezoelectric behavior in relaxor based ferroelectric single crystals. *J. Appl. Phys.*, **82(4)**, 1804 (1997)
- [26]Kleemann, W., Relaxor ferroelectrics: Cluster glass ground state via random fields and random bonds. *Phys. Status. Solidi. B.* **251(10)**, 1993–2002 (2014).
- [27]Samara, G. A. The relaxational properties of compositionally disordered ABO<sub>3</sub> perovskites. *J. Phys. Condens. Matter.* **15**, R367-R411 (2003)
- [28]Falk, F. Landau Theory and Martensitic Phase Transitions. *J. Phys.Colloq.*, **43**, C4-3 (1982)
- [29]Barrett, C. R., Nix, W. D., Tetelman, A. S. The principles of Engineering Materials. Prentice Hall Inc. (1973)
- [30]Wen, Y. F., Wang, L., Liu, H. L., Son, L. Ab Initio Study of the Elastic and Mechanical Properties of B19 TiAl. *Crystals.* **7(2)**, 39 (2017)
- [31]Curtarolo, S., Hart, G., Nardelli, M. Mingo, N., Sanvito, S., Levy, O. The high-throughput highway to computational materials design. *Nature. Mater.*, **12**, 191–201 (2013)
- [32]Choudhary, K., Garrity, K.F., Sharma, V. et al. High-throughput density functional perturbation theory and machine learning predictions of infrared, piezoelectric, and dielectric responses. *npj Comput. Mater.* **6**, 64 (2020).
- [33]Li, R. X., Li, X., Xi, L. L., Yang, J., Singh, D. J., Zhang, W. Q. High-Throughput Screening for Advanced Thermoelectric Materials: Diamond-Like ABX<sub>2</sub> Compounds. *ACS Appl. Mater. Interfaces.*, **11(28)**, 24859-24886 (2019)
- [34]Choudhary, K. Garrity, K. F., Jiang, J., Pachter. R., Tavazza, F. Computational search for magnetic and non-magnetic 2D topological materials using unified spin-orbit spillage screening. *npj Comput. Mater.*, **6**, 49 (2020)
- [35]Lich, L. V. Shimada, T. Miyata, K., Nagano, K., Wang, J., Kitamura, T. Colossal magnetoelectric effect in 3-1 multiferroic nanocomposites originating from ultrafine nanodomain structures. *Appl. Phys. Lett.*, **107**, 232904 (2015)
- [36]Shen, Z. H., Wang, J. J., Lin, Y. H., Nan, C. W., Chen, L. Q., Shen, Y. High-Throughput Phase-Field Design of High-Energy-Density Polymer Nanocomposites. *Adv. Mater.*, **30(2)**, 1704380 (2018)
- [37]Shen, Z. H., Shen, Y., Cheng, X. X., Liu, H. X., Chen, L. Q., Nan, C. W. High-throughput data-driven interface design of high-energy-density polymer nanocomposites. *J. Materiomics.*, **6(3)**, 573-581 (2020)
- [38]Liu, J. P., Wang, Y. D., Hao, Y. L., Wang, Y., Nie, Z. H., Wang, D., Ren, Y., et al. New intrinsic mechanism on gum-like superelasticity of multifunctional alloys. *Sci. Rep-UK.*, **3**, 2156 (2013)
- [39]Gao, Y., Shi, R., Nie, J. F., Dregia, S. A., Wang, Y. Group theory description of transformation pathway degeneracy in structural phase transformations, *Acta. Mater.*, **109**, 353-363 (2016)
- [40]Zheng, Y. F., Williams, R. E. A., Nag, S., Banerjee, R., Fraser, H. L., Banerjee, D. The effect of alloy composition on instabilities in the  $\beta$  phase of titanium alloys. *Scripta. Mater.*, **116**, 49-52 (2016)
- [41]Chen, L. Q. Phase-Field Models for Microstructure Evolution. *Annu. Rev. Mater. Res.*, **32**,113-140

---

(2002)

- [42] Cahn, J., Allen, S. A Microscopic Theory for Domain Wall Motion and Its Experimental Verification in Fe-Al Alloy Domain Growth Kinetics. *J. Phys. Colloq.*, **38(C7)**, 51-54 (1977)
- [43] Wang, Y., Khachaturyan, A. G. Three-Dimensional Field Model and Computer Modeling of Martensitic Transformations. *Acta. Mater.*, **45(2)**, 759-773 (1997)
- [44] Guo, S., Shi, Y., Wu, R., Liu, H., Zhao, X. Deformation behavior of a novel sandwich-like TiNb/NiTi composite with good biocompatibility and superelasticity. *Mat. Sci. Eng. A-Struct.*, **794**, 139784 (2020)
- [45] Shimada, T., Lich, L., Nagano, K., Wang, J., Kitamura, T. Hierarchical ferroelectric and ferrotoroidic polarizations coexistent in nano-metamaterials. *Sci. Rep.*, **5**, 14653 (2015)
- [46] Niessen, F., Gazder, A. A., Mithchell, D. R. G., Pereloma, E. V. In-situ observation of nucleation, growth and interaction of deformation-induced  $\alpha''$  martensite in metastable Ti-10V-2Fe-3Al. *Mat. Sci. Eng. A-Struct.*, **802**, 140237 (2021)
- [47] Hao, Y. L., Wang, H. L., Li, T., Cairney, J. M., Ceguerra, A. V., Wang, Y. D., et al. Superelasticity and Tunable Thermal Expansion across a Wide Temperature Range. *J. Mater. Sci. Technol.*, **32(8)**, 705-709 (2016)
- [48] Inamura, T., Kim, J. I., Kim, H. Y., Hosoda, H., Wakashima, K., Miyazaki, S. Composition dependent crystallography of  $\alpha''$  martensite in Ti-Nb-based  $\beta$ -titanium alloy. *Philos. Mag.*, **87(23)**, 3325-3350 (2007)
- [49] Kim, H. Y., Satoru, H., Kim, J. I., Hosoda, H., Miyazaki, S. Mechanical properties and shape memory behavior of Ti-Nb alloys. *Mater. Trans.*, **45**, 2443-2448 (2007)
- [50] Breiman, L. Random Forest. *Mach. Learn.*, **45**, 5-32 (2001)
- [51] Zhang, Y. W., Li, S. J., Obbard, E. G., Wang, H., Wang, S. C., Hao, Y. L., Yang, R. Elastic properties of Ti-24Nb-4Zr-8Sn single crystals with bcc crystal structure. *Acta. Mater.*, **59(8)**, 3081-3090 (2011)